

H-alpha features with hot onsets. II. A contrail fibril

R. J. Rutten^{1,2} and L. H. M. Rouppe van der Voort²

¹ Lingezicht Astrophysics, 't Oosteneind 9, 4158 CA Deil, The Netherlands

² Institute of Theoretical Astrophysics, University of Oslo, P.O. Box 1029, Blindern, N-0315 Oslo, Norway

Received 15 October 2015 / Accepted 22 September 2016

ABSTRACT

The solar chromosphere observed in H α consists mostly of narrow fibrils. The longest typically originate in network or plage and arch far over adjacent internetwork. We use data from multiple telescopes to analyze one well-observed example in a quiet area. It resulted from the earlier passage of an accelerating disturbance in which the gas was heated to high temperature as in the spicule-II phenomenon. After this passage a dark H α fibril appeared as a contrail. We use Saha-Boltzmann extinction estimation to gauge the onset and subsequent visibilities in various diagnostics and conclude that such H α fibrils can indeed be contrail phenomena, not indicative of the thermodynamic and magnetic environment when they are observed but of more dynamic happenings before. They do not connect across internetwork cells but represent launch tracks of heating events and chart magnetic field during launch, not at present.

Key words. Sun: activity – Sun: atmosphere – Sun: magnetic fields

1. Introduction

In the Balmer H α line at 6563 Å the solar chromosphere shows canopies of long thin features called fibrils. They occur everywhere where there is some magnetic activity. Understanding the chromosphere necessitates understanding these. Here we show a case where this requires identifying preceding events and suggest that not doing so resembles studying jet contrails in our sky without appreciating they were made by aircraft.

The literature on H α fine structure is vast (e.g., the landmark thesis of Beckers 1964 and the review by Bray & Loughhead 1974). We therefore limit our introductory summary to various types of H α fibrils and only to recent and pertinent results.

Dynamic fibrils. The name was given by Hansteen et al. (2006) and De Pontieu et al. (2007a) who after decades of slack progress since Beckers' thesis identified and explained a particular H α fibril type. These are fairly short dark fibrils that jut out in phased rows from plage and active network, representing field-guided acoustic shock waves sloshed up by the p -mode interference pattern into relatively tenuous magnetic field bundles. Short dynamic fibrils are similar but occur in sunspot chromospheres (Rouppe van der Voort & de la Cruz Rodríguez 2013; Yurchyshyn et al. 2014).

Spicules-II, RBEs, RREs. Spicules-II discovered by De Pontieu et al. (2007b) are long, slender, highly dynamic jets jutting out from the limb, with much dynamics attributed to multiple Alfvénic wave modes (e.g., De Pontieu et al. 2007c, 2012; McIntosh et al. 2008). Their manifestations on the disk are slender jet-like Doppler-shifted features observed in the wings of H α and Ca II 8542 Å as rapid blueshifted excursions (RBE) and rapid redshifted excursions (RRE) (Langangen et al. 2008; Rouppe van der Voort et al. 2009; Sekse et al. 2012, 2013). Their tops get very hot (De Pontieu et al. 2011; Pereira et al. 2014; Rouppe

van der Voort et al. 2015; Skogsrud et al. 2015). They tend to arise from plage and active network in areas that are not too active and mainly unipolar (e.g., Fig. 2 of Rouppe van der Voort et al. 2009) and favor quiet Sun and coronal holes (Pereira et al. 2012).

Long fibrils. With this name we denote the ubiquitous slender H α structures that jut out from network and plage and reach far out over adjacent internetwork, often giving the impression of spanning from one side of a supergranulation cell to another tracing closed-field canopies. We suggest below that this interpretation is not correct and therefore do not want to call them “long closed-loop fibrils”, nor “long internetwork fibrils” because they invariably are rooted in network or plage at least on one side. We thought about “long arching fibrils” because they are generally curved, more so than dynamic fibrils, but eventually chose to simply call them long fibrils.

They are absent only in the very quietest areas (Rouppe van der Voort et al. 2007), but prominently cover the solar surface above active regions and widely around them. Overall they constitute the chromosphere as named by Lockyer (1868). Their nature remains unclear, nor whether they actually map magnetic fields as one naturally supposes when viewing their patterns. They are often interpreted as cylindrical flux tubes (e.g., Foukal 1971; Sánchez-Andrade Nuño et al. 2008), but also as sheets or warps in sheets (Judge et al. 2011; Lipartito et al. 2014) or as density corrugations (Leenaarts et al. 2012, 2015).

Here we detail the formation of a single long H α fibril which we deem potentially exemplary for the class. Our study was triggered by a study of Ellerman bomb visibilities (Rutten 2016, henceforth Pub 1) which was inspired by the 2D non-equilibrium MHD simulation of Leenaarts et al. (2007) called HION henceforth following Pub 1. The effects of dynamic hydrogen ionization in the HION atmosphere defined the following recipe to understand marked presence of H α in and after dynamical in-

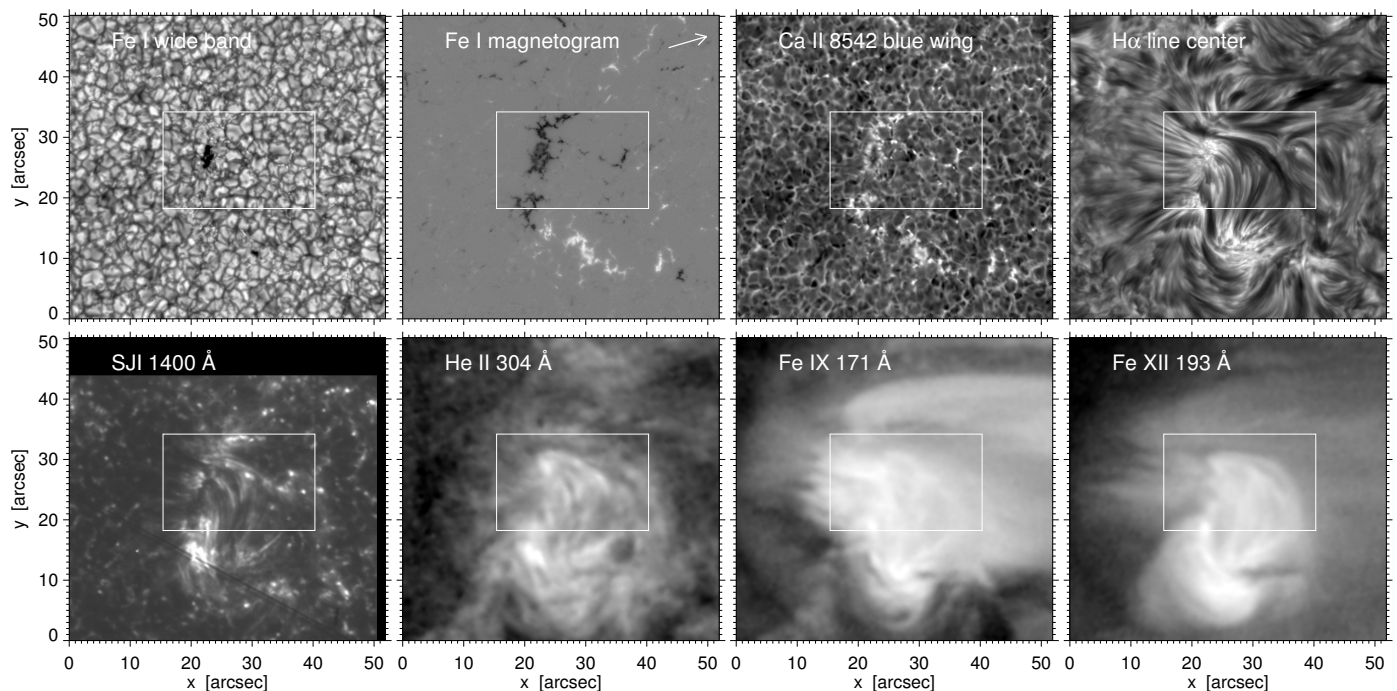


Fig. 1. Overview of the observed area at 08:22:23 UT. The field of view was centered at solar $(X, Y) = (-202, 206)$ arcsec with viewing angle $\mu = 0.95$. It is clockwise rotated with respect to (X, Y) over 62.6° . The arrow in the second panel points to disk center. *Upper row:* SST images: Fe I 6303 Å wide band, Fe I 6303 Å magnetogram, blue wing of Ca II 8542 Å at $\Delta\lambda = -0.7$ Å from line center, H α line center. *Lower row:* corresponding images from IRIS and SDO/AIA: 1400 Å slitjaw, He II 304 Å, Fe IX 171 Å, Fe XII 193 Å. The pixel sizes are 0.057 arcsec for the SST, 0.167 arcsec for IRIS, 0.6 arcsec for AIA. The white frame defines the subfield used in Fig. 2. In the fourth panel it contains the long black arching fibril discussed here.

stances with hot and dense onsets: (1) evaluate the H α extinction coefficient ($H I n=2$ level population) during the onset by assuming the Saha-Boltzmann (SB) value, (2) use the resulting large population also for cooler surrounding gas in reach of scattering Ly α radiation from the hot structure, and (3) maintain this large population subsequently during cooling and recombination.

This post-Saha-Boltzmann-extinction (PSBE) recipe holds for shocks in the HION atmosphere and was applied successfully to Ellerman bombs in Pub 1, including the suggestion that it applies partially even to the Si IV lines observed with the Interface Region Imaging Spectrograph (IRIS, De Pontieu et al. 2014) which commonly are interpreted assuming coronal equilibrium (CE). This condition is the opposite of SB equilibrium by requiring statistical equilibrium in which collisional deexcitation and recombination are fully negligible instead of fully dominating.

A corollary of Pub 1 is that other H α features with hot and dense onsets may similarly gain large SB extinction at such moments and then retain these high values during subsequent cooling. Reversely, features with unusual opaqueness in H α may represent products of hot and dense onset phenomena. Since long fibrils represent a class of H α features with intriguing opacities, we wondered whether preceding hot instances might be found producing them. The question became how to identify such precursors.

A 2014 multi-telescope campaign utilizing “last photons” of the SUMER spectrometer (Wilhelm et al. 1995) was undertaken to search for hot precursors in Lyman lines, but without success. We then found a striking example in high-resolution H α imaging spectroscopy from the Swedish 1-m Solar Telescope (SST, Scharmer et al. 2003) together with hotter diagnostics from the Atmospheric Imaging Assembly (AIA, Lemen et al.

2012) onboard the Solar Dynamics Observatory (SDO, Pesnell et al. 2012), and saw it confirmed in sharper images from IRIS. Here we present and discuss this example, which we call “contrail fibril”.

The observations are detailed in the next section. The displays combine extracts of the multiple data sets that, when viewed and blinked as multi-diagnostic movies, led to our noticing the feature. In Sect. 3 we estimate the visibilities of its onset, contrail, and aftermath. In the discussion (Sect. 4) we argue that the phenomenon shared characteristics with spicules-II and speculate about why such features become so long, what they tell us about magnetic field topography, and how ubiquitous they are. We conclude the study and outline follow-up in Sect. 5.

2. Observations

Data collection and reduction. For this study we analyzed data from a joint SST–IRIS observing campaign targeting a quiet area near solar disk center. Figure 1 gives an overview.

On June 21, 2014 the second author obtained imaging spectroscopy at the SST with the CRisp Imaging SpectroPolarimeter (CRISP, Scharmer et al. 2008) during 08:02–09:15 UT at a cadence of 11.5 s. H α was sampled at 15 wavelengths spanning ± 1.4 Å from line center, Ca II 8542 Å at 25 wavelengths spanning ± 1.2 Å from line center, Stokes-V magnetograms were obtained in Fe I 6303 Å. The reduction used the CRISPRED pipeline of de la Cruz Rodríguez et al. (2015). It included dark and flat field correction, multi-object multi-frame blind deconvolution (van Noort et al. 2005), minimization of remaining small-scale deformation through cross-correlation (Henriques 2012), pre-filter transmission correction following de la Cruz Rodríguez (2010), correction for time-dependent image rotation due to the

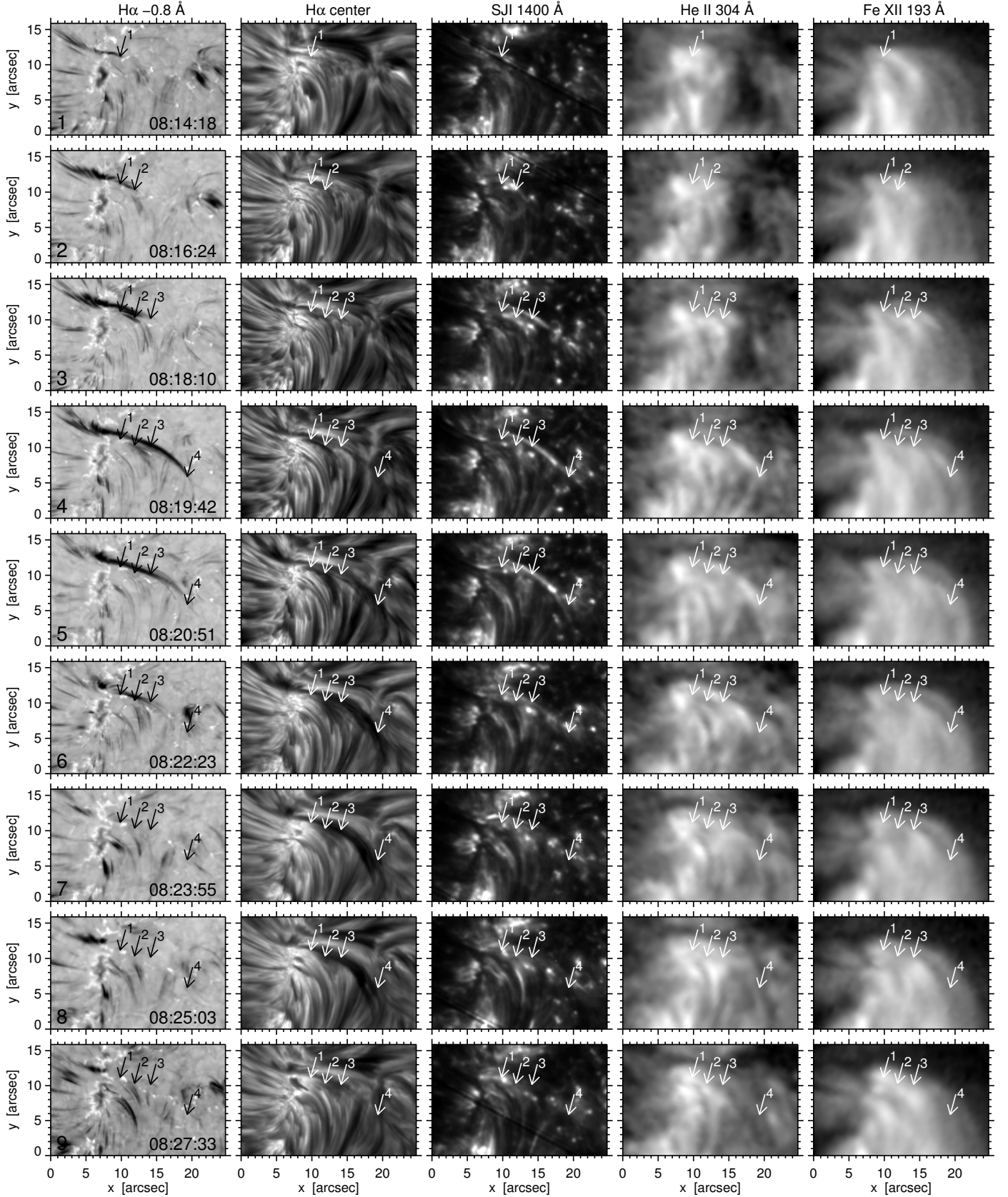


Fig. 2. Time sequence of image cutouts defined by the subfield frame in Fig. 1. The row number and the observing moment of each row are specified in the first panel of each row. *Columns:* H α images at $\Delta\lambda = -0.8$ Å from line center (SST), H α line center (SST), 1400 Å slitjaw (IRIS), He II 304 Å (AIA), Fe XII 193 Å (AIA). The four numbered arrows mark the location of the tip of the dark extending precursor streak defined successively for the first four H α blue-wing panels. Each frame is bytescaled individually. Row 6 corresponds to Fig. 1. The IRIS slit is visible in the top two and bottom two 1400 Å panels.

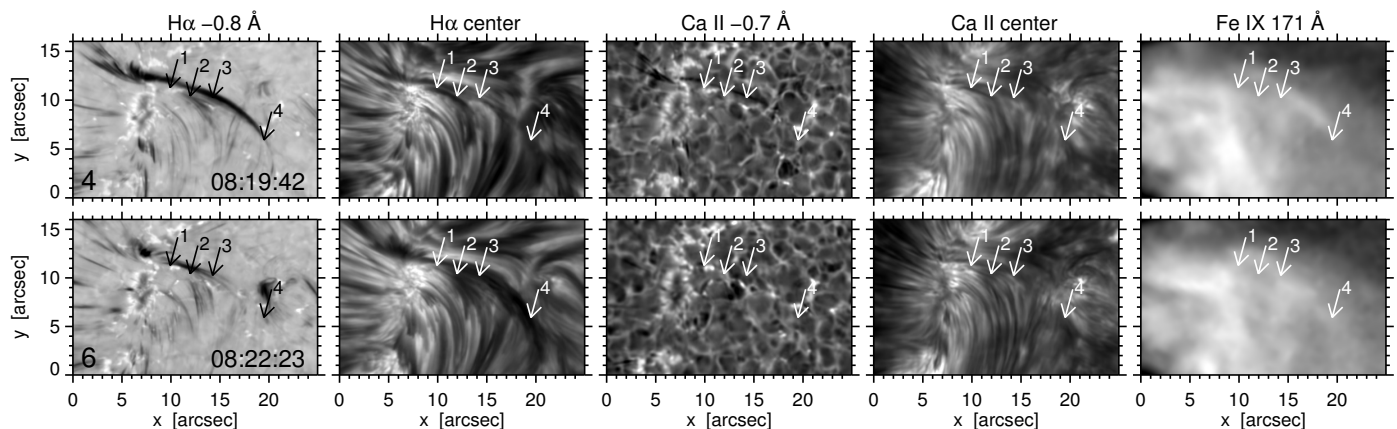


Fig. 3. Image cutouts as in Fig. 2. The first two columns repeat the first panels of rows 4 and 6 in Fig. 2. The third and fourth columns contain corresponding cutouts of Ca II 8542 Å, in the blue wing at $\Delta\lambda = -0.7$ Å from line center and at line center. The last column contains corresponding cutouts from Fe IX 171 Å (AIA).

alt-azimuth telescope configuration, and removal of remaining rubber-sheet distortions by destretching (Shine et al. 1994).

The same region was observed with IRIS. Unfortunately, its scanning spectrograph slit missed the feature described here so that we only use slitjaw images in the 1400 Å passband. These are dominated by the Si IV doublet at 1394 Å and 1403 Å in high-temperature gas (e.g., Vissers et al. 2015).

In addition, we collected corresponding image sequences from SDO. All image sequences were rotated to the SST image orientation and precisely co-aligned using interpolation of the space-based images to the spatial and temporal grid of the SST images. This was done with the SolarSoft library and IDL programs available on the [website of the first author](#).

The PSBE recipe defined in Pub 1 led us to search for features with large Hα extinction that follow on hot-onset precursors. While inspecting the SST and AIA diagnostics using the CRISP Spectral Explorer (CRISPEX; Vissers & Rouppe van der Voort 2012) as browser to compare and blink time-delay movies, we quickly noted that the prominent dark Hα fibril in Fig. 1 was preceded minutes earlier by a fast-moving bright blob in He II 304 Å and that the Hα fibril outlined the passage of this disturbance. Subsequently, we found that the latter was mapped very well in the outer blue wing of Hα. When we then co-aligned the 1400 Å slitjaw images from IRIS we found brightening that clearly tracks the same disturbance. Figures 1–3 present the phenomenon.

Field of view. Figure 1 shows the observed region. It was very quiet, far from AR 12093 and AR 12094 on the Southern hemisphere. The first panel shows that it contained only a small pore besides granulation and tiny magnetic network concentrations in intergranular lanes. At the SST resolution the latter appear as bright points even in the continuum (we invite the reader to zoom in per pdf viewer). The magnetogram in the second panel shows that these together constituted fairly dense patches of active network. The other diagnostics show corresponding brightness features.

The blue wing of Ca II 8542 Å (third panel) maps magnetic concentrations as enhanced brightness and elsewhere displays reverse granulation in the mid photosphere (Rutten et al. 2011). The Hα core samples the fibrillar chromosphere. In this quiet field long fibrils extend from the network patches but are less ubiquitous elsewhere. Some seem to connect the main opposite-

polarity patches across the center of the field, but our feature, the large black fibril within the overlaid frame, does not reach that far. Elsewhere, notably in the lower-left corner, the Hα image shows non-fibrillar swirly brightness patterns which probably represent acoustic shock patterns (Rutten et al. 2008).

The diagnostics in the lower row show increasingly diffuse brightness response to the enhanced network areas. The 1400 Å panel shows largest brightness near the polarity reversal between the main field concentrations, possibly from earlier reconnection, and elsewhere bright points as the ones ascribed to acoustic shocks by Martínez-Sykora et al. (2015).

The three AIA panels show a larger brightness blob above the network patches indicating heating of the higher atmosphere. There are similarities, even in fine structure, between He II 304 and Fe II 193 Å and more diffuse veiling originating further to the left that seems to cover this fine structure in Fe II 193 Å and yet more in Fe IX 171 Å.

Precursor and contrail. Figure 2 details the dark Hα line-center fibril that we call the “contrail fibril” and is the topic of this study. It is prominent in the second column in rows 5–8, longest in row 6. It is much weaker or absent in the preceding rows, but the blue-wing images in the first column show a long, slender, growing dark feature at the same location with bright counterparts in the IRIS and AIA columns.

The action started with a fan of RBE extensions near the foot of the contrail fibril. It first shot off a long RBE towards the upper left, sampled in the first panel of Fig. 2. Unfortunately, the IRIS slit had just passed (dark slanted line in the top 1400 Å panel).

Subsequently, the dark extensions seen in the second Hα-wing panel (we again invite the reader to zoom in per pdf viewer) fanned out progressively in shooting off growing RBEs from left to right as in a peacock tail display, finally sending off the long precursor of our contrail fibril towards the right. The latter’s extension progress is marked by the four arrows. Each was placed successively at the tip of the growing dark blue-wing feature in rows 1–4. The Hα profiles in Fig. 4 are for these four locations.

The second arrow actually identifies the tip of another RBE shot off in parallel to the main one pointed at later by arrows 3 and 4. This was also a precursor: it later produced its own, shorter, and more curved contrail (dark fibril in Hα line center in rows 4–6). We call this contrail B.

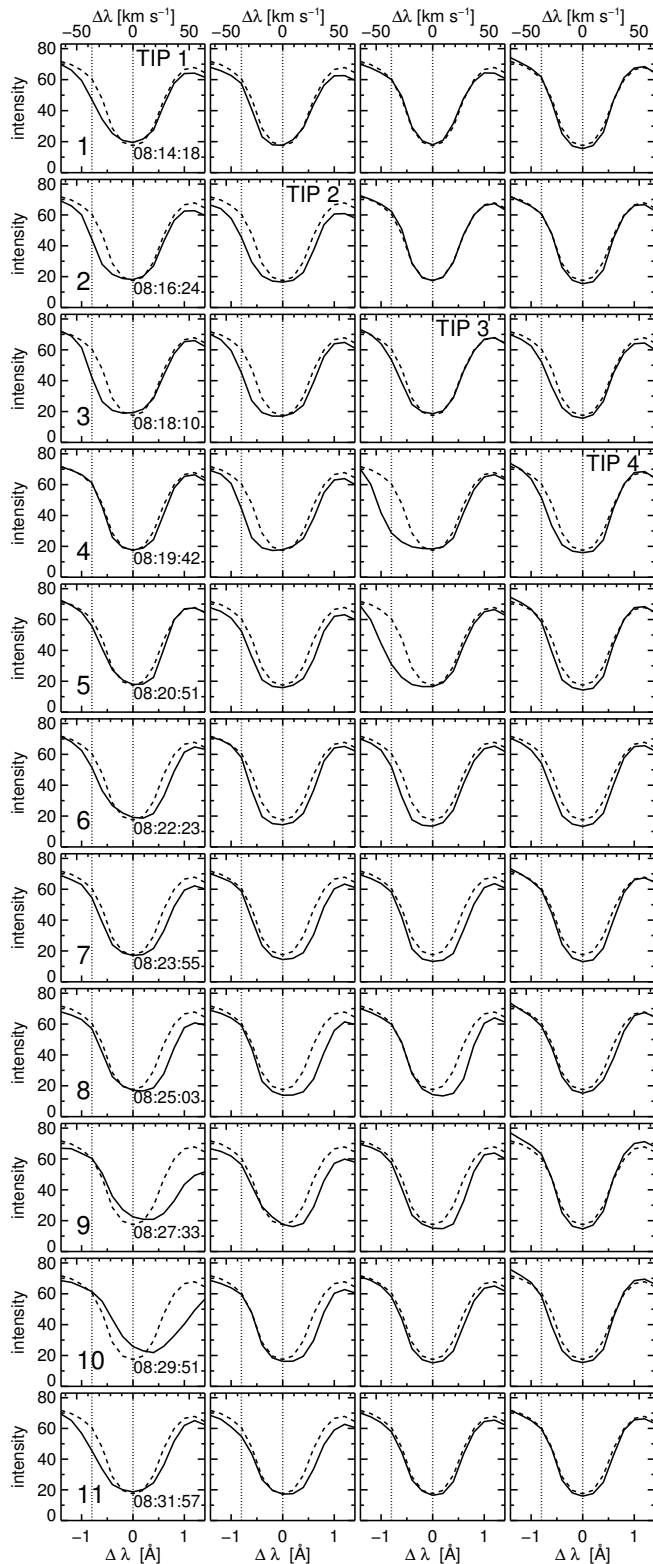


Fig. 4. $H\alpha$ profiles at the four locations marked by arrows in Fig. 2. The wavelength separation from line center is given in Å at the bottom, in km s^{-1} at the top. The intensity scale is arbitrary. The first nine rows are the same time samplings and have the same numbers as in Fig. 2, similarly specified in the first column. The last four rows are for the same times as in Fig. 5. The columns correspond to the initial precursor-tip locations marked by the four arrows in Fig. 2. The panels for their defining moment are labeled “TIP” in the first four rows. *Solid*: $H\alpha$ profile at this location and time. *Dashed*: mean profile of the whole sequence for reference, identical in all panels. *Dotted, vertical*: sampling wavelengths used in Fig. 2.

The mean proper motion speeds over the surface defined by the arrow-marked tip locations of the main dark streak in the initial blue-wing images in the first column of Fig. 2 are 13, 15, and 53 km s^{-1} for 1→2, 2→3, and 3→4, respectively. It accelerated appreciably. The last value is similar to the speeds reached by RBEs (Rouppe van der Voort et al. 2009), but this streak was much longer when it reached 15-arcsec extension five minutes after its launch (row 4; observing times are specified in the first column).

The dark fibril at the center of $H\alpha$ appeared a minute later and lasted four minutes (second column, rows 5–8). It faithfully mapped the precursor shape and therefore represents a post-passage contrail.

Actually, we first noted the extending precursor in the $\text{He II } 304 \text{ Å}$ sequence (fourth column) where it is most clearly evident in rows 3–6. We then recognized its presence (when you know what to look for) also in the $\text{Fe IX } 171 \text{ Å}$ and $\text{Fe XII } 193 \text{ Å}$ images. We sample only the latter in Fig. 2 in order not to make its panels too small, but Fig. 3 shows the corresponding $\text{Fe IX } 171 \text{ Å}$ cutouts at the times of rows 4 and 6 of Fig. 2.

Only afterwards we noted the slender precursor in the $H\alpha$ wing images and realized from inspecting the $H\alpha$ profiles with CRISPEX that it is so dark from RBE signature including large line broadening. This is detailed with profile samples in Fig. 4.

Later we co-aligned the IRIS images and found that the precursor is very evident in the 1400 Å slitjaw images (third column of Fig. 2). In rows 3–5 it appears as a very thin extending streak starting at location 3 and extending to but not reaching location 4. An underlying bright point, also present before and after, was enhanced by the streak which implies optically thin formation of the Si IV lines in the streak and therefore direct imaging of intrinsic fine structure, in particular the narrow precursor width.

Figure 2 shows that the precursor became hotter along its track. The 1400 Å and hotter diagnostics do not show its start from location 1 to location 3 in rows 1–3, only the part from 3 to 4 in rows 4–6, but in 1400 Å the streak does not reach location 4. In $\text{He II } 304 \text{ Å}$ and $\text{Fe XII } 193 \text{ Å}$ the streak is most evident closer to location 4 (row 4), and well-evident in $\text{Fe IX } 171 \text{ Å}$ between these locations (Fig. 3). This suggests increasing ionization along the track to very high degree, with Si IV peaking closer to location 3 and the highest iron stage closest to location 4.

In summary, a sudden event in the low atmosphere sent off a disturbance that heated gas along its path to very high temperature.

By row 6, seven minutes after its onset, the precursor became invisible, but by then had left the black fibril at $H\alpha$ line center along its wake. This contrail persisted three more minutes.

By 08:27 UT (row 9) the show was over in these high-temperature diagnostics – just when the IRIS slit was nearing in the next scan (bottom 1400 Å panel). It is a pity that the scan timing missed the Si IV emission streak in rows 4–6 because the slit happened to be aligned with its direction.

Comparison with $\text{Ca II } 8542 \text{ Å}$. Figure 3 adds cutout images in $\text{Ca II } 8542 \text{ Å}$ and $\text{Fe IX } 171 \text{ Å}$ for key moments in Fig. 2: the time when the precursor streak reached its maximum length in the blue wing of $H\alpha$ (row 4) and nearly three minutes later (row 6) when the line-center contrail fibril reached maximum visibility. The $\text{Ca II } 8542 \text{ Å}$ wing image shows the first part of the precursor streak, but not beyond location 3. The contrail fibril is not evident at all in $\text{Ca II } 8542 \text{ Å}$.

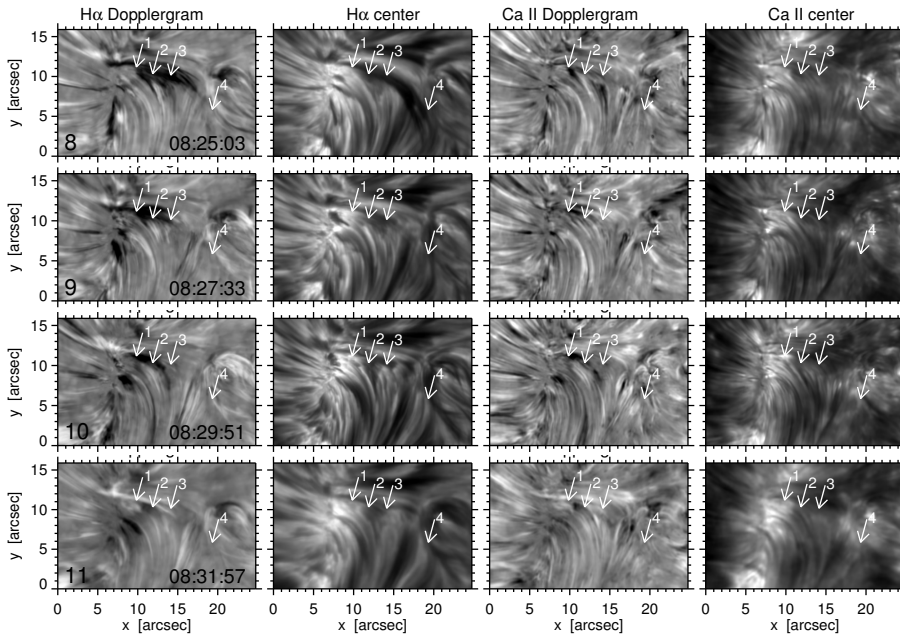


Fig. 5. Time sequence of aftermath image cutouts as in Fig. 2. *Columns:* $H\alpha$ Dopplergrams at $\Delta\lambda = \pm 0.6 \text{ \AA}$ with black denoting redshift. $H\alpha$ images at line center, $\text{Ca II } 8542 \text{ \AA}$ Dopplergrams at $\Delta\lambda = \pm 0.3 \text{ \AA}$, $\text{Ca II } 8542 \text{ \AA}$ images at line center. The first two rows are for the same moments as the last two rows in Fig. 2 and share their numbers. The intensity images are bytescaled individually but the Dopplergrams have identical greyscales along columns.

H-alpha profiles. Figure 4 shows $H\alpha$ profiles for the locations defined by the four arrows in Fig. 2 and at the same sampling times, so with the same row numbers and time labels as in Fig. 2. The four panels labeled TIP in the first four rows correspond to the location defining times in Fig. 2 marking how far the extending precursor streak had reached in the $H\alpha$ blue-wing images. Each tip profile shows characteristic RBE shape with substantial core broadening on the blue side. This signature increased at all four locations for some minutes after the tip definition, in particular at location 3.

Generally, $H\alpha$ broadening suggests temperature increase with less influence from nonthermal line broadening than for other lines due to the small atomic weight of hydrogen (Cauzzi et al. 2009). Such profiles therefore indicate heating plus updraft.

The RBE signature vanished by row 6, leaving just hotter and darker profiles than average when the precursor lost its visibility in the blue wing of $H\alpha$ and in the IRIS and SDO images. The heating event had passed and left cooling gas with large $H\alpha$ opacity producing the contrail fibril at $H\alpha$ center (rows 5–8 of Fig. 2).

From row 7 most profiles show reversed Dopplershift signatures detailed in the next paragraph.

Cooling aftermath. Rows 7–11 of Fig. 4 show first increasing and then decreasing high-temperature-plus-redshift signature for locations 1–3. In rows 7 and 8 it was largest at location 2 but in rows 9–10 it became rather outrageous at location 1. This suggests an aftermath in which kicked-up heated gas moved back down while recombining and becoming invisible in the hotter diagnostics. Since hydrogen recombination takes much energy the gas cooled drastically and at about 10% neutral passed into the regime with retarded hydrogen recombination below 7000 K as in the fundamental 1D non-equilibrium simulation of Carlsson & Stein (2002) and in the post-shock gas in the 2D HION atmosphere. During this retarded phase the cooling gas maintained large $H\alpha$ hot-precursor opacity. This is confirmed by the cutout images in Fig. 5 which show a retracting feature with large redshift. Only its base between locations 1 and 2 became visible also in the $\text{Ca II } 8542 \text{ \AA}$ Dopplergrams, best in row 10, at smaller opacity.

Both line centers brightened at location 1 in rows 9 and 10 of Fig. 5 from the Dopplershift evident in the first column of Fig. 4.

In the final row of Fig. 5 the gas at location 1 was still unusually hot (Fig. 4), but already showed blueshift due to a new heating agent drawing a thin bright streak from left to right in the Dopplergrams. It just missed the other sampling locations. This streak became visible also in the IRIS 1400 \AA images, extended to 15 arcsec length, and two minutes later produced a long $H\alpha$ line-center fibril much as the one presented which was also followed by a contracting redshift feature. It was very similar to our contrail except slenderer. We call it contrail C.

Conclusion of this section. If one had noted the dark $H\alpha$ fibril when it was most prominent, in rows 6–8 of Fig. 2, and tried to model that (say with cloud modeling) without being aware of the hot precursor in rows 3–5, then one would be as mistaken as when interpreting jet contrails in the sky without knowing about jet engines. It was an intrinsically dynamic phenomenon starting with a fierce jet-like heating agent producing gas at very high temperature which subsequently recombined and cooled, became visible at the center of $H\alpha$, and partly flowed back. Also a jet contrail, but from a solar jet and recombination rather than condensation.

3. Interpretation

In this section we do not try to interpret the nature and mechanism of the heating event but address the visibilities of the precursor, contrail, and aftermath.

PSBE estimation. One would not expect to see the same feature in $H\alpha$, He II , Si IV , Fe IX and Fe XII simultaneously, but in rows 4 and 5 of Fig. 2 the onset streaks correspond fairly closely between these diagnostics. Obviously, they are due to some process causing large heating (Sect. 4). It was initiated along the row of dark extensions in the $H\alpha$ blue-wing image in row 2 of Fig. 2 in the low atmosphere, implying dense gas for the onset. The combination of hot and dense makes the PSBE recipe of Pub 1 appropriate for explaining the joint precursor visibilities in these

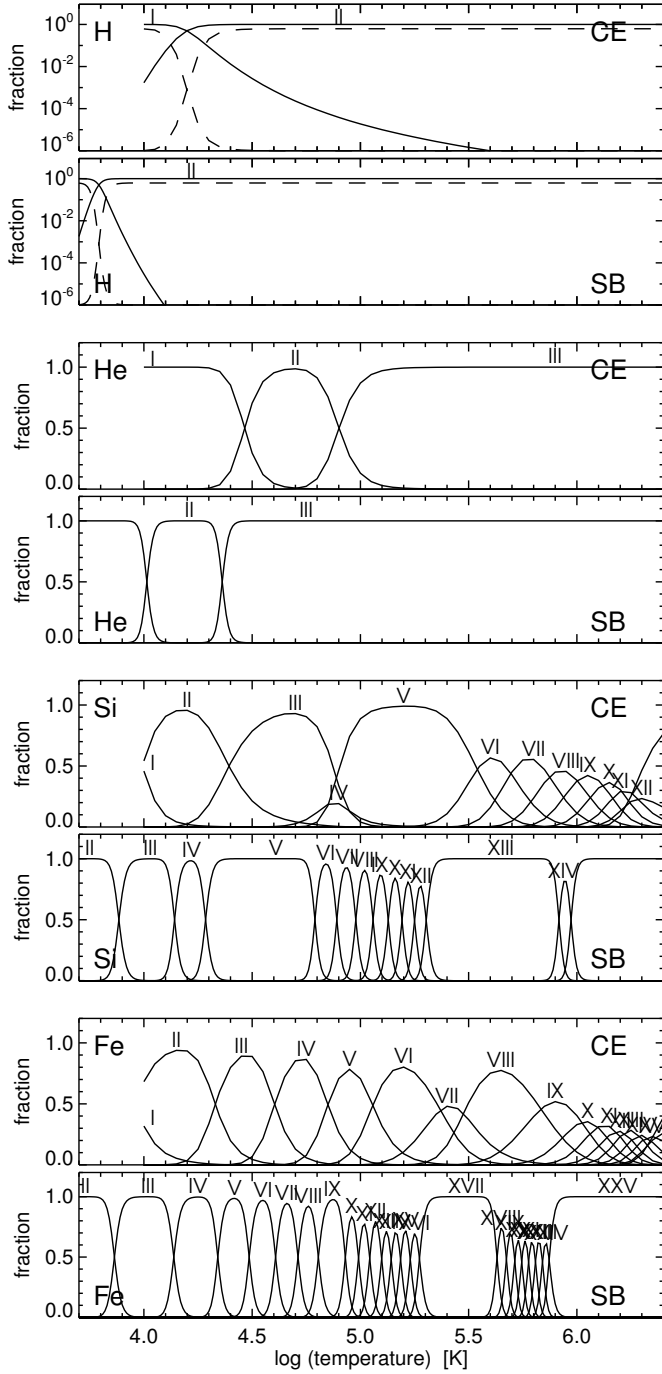


Fig. 6. CE/SB ionization-stage population comparisons for H, He, Si and Fe. *Upper panel of each pair:* CE distribution with temperature. *Lower panel of each pair:* SB distribution with temperature for fixed electron density $N_e = 10^{14} \text{ cm}^{-3}$. For lower N_e the SB curve patterns remain similar but the flanks steepen and the peaks shift leftward (about -0.05 in $\log(T)$ for tenfold N_e reduction). The first pair for hydrogen has logarithmic y -axes; the dashed curves are on the linear scales of the other panels.

very disparate diagnostics and the subsequent appearance of the $H\alpha$ line-center contrail and its aftermath.

The recipe employs Figs. 6 and 7. They resemble Figs. 4 and 5 of Pub 1 and were made as described there. Figure 6 compares CE ionization distributions with their SB counterparts over a wide temperature range. Figure 7 quantifies SB extinction coefficients for the specified lines as function of temperature, for total

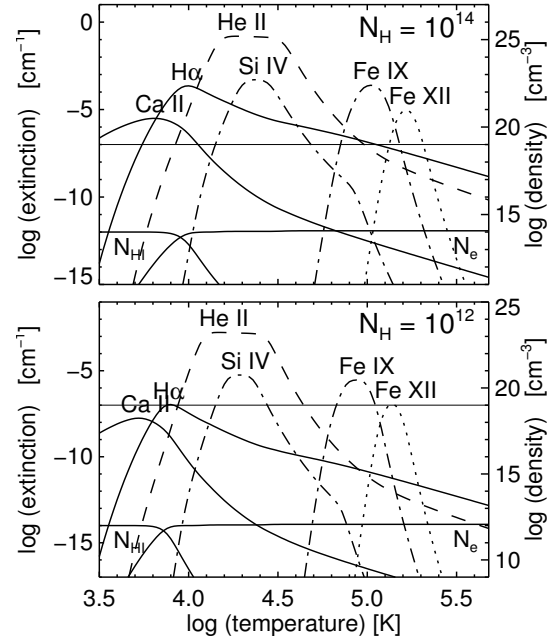


Fig. 7. SB extinction α' for $H\alpha$ (solid), $\text{Ca II } 8542 \text{ \AA}$ (solid), $\text{He II } 304 \text{ \AA}$ (dashed), $\text{Si IV } 1394 \text{ \AA}$ (dot-dashed), $\text{Fe IX } 171 \text{ \AA}$ (dot-dashed) and $\text{Fe XII } 193 \text{ \AA}$ (dotted) as function of temperature, for total hydrogen densities $N_H = 10^{14}$ and 10^{12} cm^{-3} (upper and lower panel, respectively). The two cross-over solid curves near the bottom are the competing neutral hydrogen and electron density, with scales on the right. The extinction scales at left and the density scales at right shift upward between the panels to compensate for the density decrease. The horizontal line at $\log \alpha' = -7$ marks optical thickness unity for a slab of 100 km geometrical thickness.

hydrogen densities corresponding to heights 850 and 1520 km in the chromosphere of the ALC7 standard model of Avrett & Loeser (2008).

Figure 6 quantifies the large differences in the temperatures at which successive ionization stages of the plotted elements reach maximum presence between the SB and CE extremes. For example, the IRIS Si IV lines typically form at 80 000 K in CE but at 16 000 K when SB holds. Such pair comparison defines the range from SB validity at very high density to CE validity at very low density.

SB extinction can be valid in momentary hot and dense instances at chromospheric heights where generally NLTE is the rule. When the gas becomes so hot that hydrogen ionizes substantially, the resulting large boost of the electron density may create collisionally constrained SB populations at sufficiently high gas density and feature thickness. This then holds usually only for lower levels of resonance lines, not for their upper levels because these suffer NLTE photon losses.

$H\alpha$ is a special case because it rides on top of $\text{Ly}\alpha$ in which even a small neutral-hydrogen feature can be sufficiently opaque to thermalize $\text{Ly}\alpha$ radiation notwithstanding the very small $\text{Ly}\alpha$ collision rates. This is the case throughout the ALC7 chromosphere (Fig. 1 of Pub 1) and also within the HION shocks. In the latter the $H\alpha$ extinction reaches the SB value at electron densities as low as 10^9 cm^{-3} thanks to 10% hydrogen ionization producing 10^3 more electrons than available from the electron-donor metals in cooler gas (Fig. 2 of Leenaarts et al. 2007).

SB extinction is also a good assumption for $\text{Ca II } 8542 \text{ \AA}$ (Pub 1) and applies to resonance lines of majority species wherever the Saha law applies, which at high density is more likely

than CE. Therefore, the curves for $H\alpha$ and $\text{Ca II } 8542 \text{ \AA}$ in Fig. 7 are probably correct where they peak, whereas the temperature locations of the peaks for the higher ions represent lower limits only. However, even for these peaks shifts as far to the right as predicted by CE (Fig. 6) are unlikely.

Precursor visibilities. The $H\alpha$ curves in Fig. 7 are for line center. For the $H\alpha$ wing visibility they should be shifted down over about one logarithmic unit and so get significantly below the horizontal line in the lower panel. The choice of a 100-km slab as geometrical feature thickness is arbitrary. The width of the blue-wing precursor in the first column of Fig. 2 measures about 1 arcsec or 700 km but this is widened by resonance scattering in $\text{Ly}\alpha$ (Pub 1). The intrinsic precursor width shown by the 1400 \AA panels is sub-arcsecond. The 100-km line should therefore be a reasonable visibility indicator.

Because the $H\alpha$ curves drop less steeply than the others $H\alpha$ may still reach overlap visibility with He II and Si IV as predicted in the upper panel of Fig. 6 and observed in the first, third and fourth panels of row 4 of Fig. 2 (remember that both extinction and emissivity scale with the lower-level population). Since the initial part of the $H\alpha$ -wing precursor is not visible in these hotter diagnostics it started well below 15 000 K but then became much hotter.

The $\text{Ca II } 8542 \text{ \AA}$ visibility constrains the initial temperature of the precursor to yet lower values. The curves for this line and for $H\alpha$ in Fig. 7 cross at $T \approx 6000 \text{ K}$ with nearly opposite temperature sensitivity. The precursor start near location 1 shows similar morphology at the two line centers in Fig. 3, suggesting temperature well below 10 000 K, but beyond location 3 the precursor is invisible in $\text{Ca II } 8542 \text{ \AA}$, suggesting temperature around or above 10 000 K. The subsequent contrail also remained invisible (Figs. 3 and 5).

The Fe-line humps in Fig. 7 are around $T = 10^5 \text{ K}$. Since the precursor tip showed up in them it must have become very hot, even if it did not become CE hot ($T \approx 10^6 \text{ K}$). The observations in these lines (Figs. 2 and 3) show best precursor visibility near location 4 at the time of row 4, but the precursor also reached that far in $\text{He II } 304 \text{ \AA}$ and in the blue wing of $H\alpha$. This joint visibility suggests temperature around 10^5 K at hydrogen density around 10^{14} cm^{-3} , yet hotter for conditions closer to CE.

Contrail and aftermath visibilities. The PSBE recipe also explains the appearance of the dark fibril at $H\alpha$ line center well after the passage of the heating event. The latter ionized hydrogen instantaneously but hydrogen recombination in the subsequent cooling gas was retarded. While the gas cooled to below 10^4 K the $H\alpha$ extinction did not slide down the steep SB slopes in Fig. 7 instantaneously, but instead stayed near the peak value passed at about 7000 K during multiple minutes. Figure 4 shows that this relaxation happened first at location 4 and progressively later at the lower-number locations along which the heated gas came back down during the aftermath.

At location 1 near the base of the heating event in the low atmosphere the cooling was largest and took the longest. There the temperature lowered sufficiently for $\text{Ca II } 8542 \text{ \AA}$ Doppler-shift visibility (Fig. 5). The $\text{Ca II } 8542 \text{ \AA}$ curves in Fig. 7 peak near 5000 K; at such temperatures the instantaneous $H\alpha$ extinction is very much lower, but retardation kept the actual $H\alpha$ opacity higher as evident in Fig. 5.

Conclusion of this section. The PSBE recipe applies well to the contrail phenomenon. It explains that the precursor was observed simultaneously in the very disparate diagnostics in Fig. 2 but only its start in $\text{Ca II } 8542 \text{ \AA}$, that a large dark subsequent contrail fibril followed in the center of $H\alpha$, and that the cooling returning aftermath cloud retained large $H\alpha$ opacity while eventually becoming visible in $\text{Ca II } 8542 \text{ \AA}$.

4. Discussion

Nature of the event. The onset was much like the start of a regular RBE. Indeed, the detection criteria of Rouppe van der Voort et al. (2009) would have classified this feature as an RBE. The main difference is that its track is so long and that it later got outlined by the subsequent contrail fibril over such long length. We speculate that the precursor was essentially a spicule-II phenomenon but directed more horizontally than in regular RBEs and RREs and possibly from a fiercer heating agent. It originated in a similarly quiet area as in Rouppe van der Voort et al. (2009) and speeded up and got as hot as spicules-II do on their way up, while its lower part returned similarly to the surface (cf. De Pontieu et al. 2011; Pereira et al. 2014).

The mechanism that shoots off spicules-II and their on-disk RBE and RRE counterparts remains unknown (Pereira et al. 2012). Since they often originate in unipolar network, direct bipolar strong-field reconnection seems unlikely. The peacock fan sequence that sent off our contrail fibril and contrail B does suggest reconnection, perhaps component or fly-by reconnection as in Meyer et al. (2012). It resembles the fan of peacock jets in an umbral light bridge reported by Robustini et al. (2016), but that was probably bipolar reconnection.

The other driver option is local generation of Alfvénic waves. Spicules-II combine jet production with Alfvénic swaying and torsion modes (e.g., De Pontieu et al. 2012; Sekse et al. 2013); the onset of our feature likely harbored the same. We speculate that its very long length was contributed particularly by a vorticity kick since torsion waves are uncompressive and can travel far before dissipation by mode coupling.

There is also the issue whether the precursor was a bullet-like hot blob or a jet-like heating agent that extended in length. The long thin shape of the precursor in Fig. 2 suggests the latter, but He II and Si IV have large valence-electron jumps in their previous ionization stages which may produce retarded recombination similarly to hydrogen (in which it is caused by the $\text{Ly}\alpha$ jump, see Carlsson & Stein 2002; for helium retardation see Golding et al. 2014). Long tracks may then also appear in these diagnostics from cooling gas after a hot-bullet passage.

Finally, the sequential visibility of the precursor track, contrail fibril, and aftermath suggest that the latter consisted of cooling gas in which hydrogen recombined.

Contrail ubiquity. An obvious issue is whether the contrail fibril presented here is an uncommon or a common phenomenon. We do not answer this question here because it requires detailed analysis of multiple datasets, sampling different levels of activity; we prefer to postpone such larger-volume studies to future reports. However, naturally we have searched the present dataset for similar instances and cursorily inspected other SST datasets as well. The easiest way is to blink $H\alpha$ line-center movies with varying time delay against $H\alpha$ blue-wing movies with CRISPEX, which permits time-delay different-wavelength movie blinking with simultaneous profile displays.

The upshot is that, in addition to contrails B and C which occurred already within the small cutout field during the short period presented here, we quickly found more but also that not every long H α fibril has an easily identifiable hot precursor. We have the impression that it helped much that the present field of view was very quiet, so that our contrail fibril stood out without interference from neighboring others in place and time. Areas with denser fibril canopies present so much time-dependent confusion that it becomes very difficult to identify precursors and resulting contrails uniquely and reliably.

Contrail fibrils as field mappers. The contrail fibril did not connect field from network at one side of a supergranular cell to network on the other side, although it pointed to the opposite-polarity field patch below the frame in Fig. 1. Short of the latter there was not enough opposite polarity for such short-circuiting.

Instead, the fibril delineated cooling gas after the passage of the onset disturbance; the fibril outlined its path. Line-tying of plasma charged by hydrogen ionization may well have aligned the disturbance (whether bullet or jet) initially along field lines. Whether the outlined fields indeed continued to span the internetwork and closed in the large opposite-polarity patch cannot be established from the contrail.

Also, the subsequent fibril outlined azimuthal field direction as it was a few minutes earlier. It may have suffered subsequent deformation by flows as when winds affect jet contrails; indeed, the contrail tip seems to shift away from location 4 in rows 6–8 of Fig. 2.

The resulting suggestion is twofold: (1) contrail fibrils do not visibly connect opposite polarity fields across internetwork cells; if they appear to do so this rather implies that the fields from both sides point to each other – as they do not only in closed loops but also for unipolar fields that meet and turn up halfway as in standard cartoons (including the venerable Fig. 1 of Noyes 1967), and (2) in such two-sided mapping H α fibrils do not outline the present but possibly the past field topography. Slender features in the H α wings or H α Dopplergrams and mapped yet better through optically thin line formation in 1400 Å images are better instantaneous indicators.

The memory effect adds to the incomplete rendition of field topography due to the complex interactions of the Alfvénic waves that fibrils harbor, as shown by Leenaarts et al. (2015). Their simulation did not include non-equilibrium H α synthesis, therefore lacked the H α memory of large preceding hydrogen ionization, and so underestimated the lack of fibril-field correspondence. Proper 3D non-equilibrium spectrum synthesis remains too demanding, but a quick upper estimate is to use the H α peaks in Fig. 7 by setting the H α lower-level population to $\log(n_2/N_H) = 0.683 \log(N_H) - 14.8$ (Pub 1).

5. Conclusion

We have shown how a long dark H α fibril appeared along the trajectory of a fast sudden disturbance which passed minutes before and heated gas to very high temperature along its track. This example shows that H α fibrils can represent past happenings of much fiercer nature than the fibrils themselves would suggest when interpreted through time-independent modeling of their subsequent appearance. The lesson is that the solar chromosphere is finely structured not only in space but also in time, and that at least for some features the recent past must be taken into account to understand their present presence.

Our obvious next quest is to ascertain whether all or most long H α fibrils are contrails or whether this one was an uncommon happening. We suspect it was not, but that precursor identification is less easy in fields with larger fibril crowding from more activity.

It will also be good to find contrails sampled by the IRIS slit.

Acknowledgements. We thank Tiago Pereira for his help during the observations. Comments from the referee led to considerable improvement of the presentation. IRIS is a NASA small explorer mission developed and operated by LMSAL with mission operations executed at NASA Ames Research Center and major contributions to downlink communications funded by the Norwegian Space Center through an ESA PRODEX contract. The SST is operated on the island of La Palma by the Institute for Solar Physics of Stockholm University in the Spanish Observatorio del Roque de los Muchachos of the Instituto de Astrofísica de Canarias. This research received funding from both the Research Council of Norway and the European Research Council under the European Union's Seventh Framework Programme (FP7/2007–2013) / ERC grant agreement nr. 291058. We made much use of the SolarSoft and ADS libraries.

References

- Avrett, E. H. & Loeser, R. 2008, *ApJS*, 175, 229 [ADS](#)
 Beckers, J. M. 1964, PhD thesis, Sacramento Peak Observatory, Air Force Cambridge Research Laboratories, Mass., USA [ADS](#)
 Bray, R. J. & Loughhead, R. E. 1974, *The solar chromosphere*, ed. R. J. Bray & R. E. Loughhead [ADS](#)
 Carlsson, M. & Stein, R. F. 2002, *ApJ*, 572, 626 [ADS](#)
 Cauzzi, G., Reardon, K., Rutten, R. J., Tritschler, A., & Uitenbroek, H. 2009, *A&A*, 503, 577 [ADS](#)
 de la Cruz Rodríguez, J. 2010, PhD thesis, Stockholm University [ADS](#)
 de la Cruz Rodríguez, J., Löfdahl, M. G., Sütterlin, P., Hillberg, T., & Rouppe van der Voort, L. 2015, *A&A*, 573, A40 [ADS](#)
 De Pontieu, B., Carlsson, M., Rouppe van der Voort, L. H. M., et al. 2012, *ApJL*, 752, L12 [ADS](#)
 De Pontieu, B., Hansteen, V. H., Rouppe van der Voort, L., van Noort, M., & Carlsson, M. 2007a, *ApJ*, 655, 624 [ADS](#)
 De Pontieu, B., McIntosh, S., Hansteen, V. H., et al. 2007b, *PASJ*, 59, S655 [ADS](#)
 De Pontieu, B., McIntosh, S. W., Carlsson, M., et al. 2011, *Science*, 331, 55 [ADS](#)
 De Pontieu, B., McIntosh, S. W., Carlsson, M., et al. 2007c, *Science*, 318, 1574 [ADS](#)
 De Pontieu, B., Title, A. M., Lemen, J. R., et al. 2014, *SoPh*, 289, 2733 [ADS](#)
 Foukal, P. 1971, *SoPh*, 20, 298 [ADS](#)
 Golding, T. P., Carlsson, M., & Leenaarts, J. 2014, *ApJ*, 784, 30 [ADS](#)
 Hansteen, V. H., De Pontieu, B., Rouppe van der Voort, L., van Noort, M., & Carlsson, M. 2006, *ApJL*, 647, L73 [ADS](#)
 Henriques, V. M. J. 2012, *A&A*, 548, A114 [ADS](#)
 Judge, P. G., Tritschler, A., & Chye Low, B. 2011, *ApJL*, 730, L4 [ADS](#)
 Langangen, Ø., De Pontieu, B., Carlsson, M., et al. 2008, *ApJL*, 679, L167 [ADS](#)
 Leenaarts, J., Carlsson, M., Hansteen, V., & Rutten, R. J. 2007, *A&A*, 473, 625 [ADS](#)
 Leenaarts, J., Carlsson, M., & Rouppe van der Voort, L. 2012, *ApJ*, 749, 136 [ADS](#)
 Leenaarts, J., Carlsson, M., & Rouppe van der Voort, L. 2015, *ApJ*, 802, 136 [ADS](#)
 Lemen, J. R., Title, A. M., Akin, D. J., et al. 2012, *SoPh*, 275, 17 [ADS](#)
 Lipartito, I., Judge, P. G., Reardon, K., & Cauzzi, G. 2014, *ApJ*, 785, 109 [ADS](#)
 Lockyer, J. N. 1868, *Proceedings of the Royal Society of London Series I*, 17, 131 [ADS](#)
 Martínez-Sykora, J., Rouppe van der Voort, L., Carlsson, M., et al. 2015, *ApJ*, 803, 44 [ADS](#)
 McIntosh, S. W., De Pontieu, B., & Tarbell, T. D. 2008, *ApJL*, 673, L219 [ADS](#)
 Meyer, K. A., Mackay, D. H., & van Ballegoijen, A. A. 2012, *SoPh*, 278, 149 [ADS](#)
 Noyes, R. W. 1967, in *IAU Symposium*, Vol. 28, *Aerodynamic Phenomena in Stellar Atmospheres*, ed. R. N. Thomas, 293 [ADS](#)
 Pereira, T. M. D., De Pontieu, B., & Carlsson, M. 2012, *ApJ*, 759, 18 [ADS](#)
 Pereira, T. M. D., De Pontieu, B., Carlsson, M., et al. 2014, *ApJL*, 792, L15 [ADS](#)
 Pesnell, W. D., Thompson, B. J., & Chamberlin, P. C. 2012, *SoPh*, 275, 3 [ADS](#)
 Robustini, C., Leenaarts, J., de la Cruz Rodríguez, J., & Rouppe van der Voort, L. 2016, *A&A*, 590, A57 [ADS](#)
 Rouppe van der Voort, L. & de la Cruz Rodríguez, J. 2013, *ApJ*, 776, 56 [ADS](#)
 Rouppe van der Voort, L., De Pontieu, B., Pereira, T. M. D., Carlsson, M., & Hansteen, V. 2015, *ApJL*, 799, L3 [ADS](#)
 Rouppe van der Voort, L., Leenaarts, J., De Pontieu, B., Carlsson, M., & Vissers, G. 2009, *ApJ*, 705, 272 [ADS](#)

- Roupe van der Voort, L. H. M., De Pontieu, B., Hansteen, V. H., Carlsson, M., & van Noort, M. 2007, ApJL, 660, L169 [ADS](#)
- Rutten, R. J. 2016, A&A, 590, A124 [ADS](#) (Pub 1)
- Rutten, R. J., Leenaarts, J., Roupe van der Voort, L. H. M., et al. 2011, A&A, 531, A17 [ADS](#)
- Rutten, R. J., van Veelen, B., & Sütterlin, P. 2008, SoPh, 251, 533 [ADS](#)
- Sánchez-Andrade Nuño, B., Bello González, N., Blanco Rodríguez, J., Kneer, F., & Puschmann, K. G. 2008, A&A, 486, 577 [ADS](#)
- Scharmer, G. B., Bjelksjo, K., Korhonen, T. K., Lindberg, B., & Petterson, B. 2003, in Proc. SPIE, Vol. 4853, Innovative Telescopes and Instrumentation for Solar Astrophysics, ed. S. L. Keil & S. V. Avakyan, 341–350 [ADS](#)
- Scharmer, G. B., Narayan, G., Hillberg, T., et al. 2008, ApJL, 689, L69 [ADS](#)
- Sekse, D. H., Roupe van der Voort, L., & De Pontieu, B. 2012, ApJ, 752, 108 [ADS](#)
- Sekse, D. H., Roupe van der Voort, L., De Pontieu, B., & Scullion, E. 2013, ApJ, 769, 44 [ADS](#)
- Shine, R. A., Title, A. M., Tarbell, T. D., et al. 1994, ApJ, 430, 413 [ADS](#)
- Skogsrud, H., Roupe van der Voort, L., De Pontieu, B., & Pereira, T. M. D. 2015, ApJ, 806, 170 [ADS](#)
- van Noort, M., Roupe van der Voort, L., & Löfdahl, M. G. 2005, SoPh, 228, 191 [ADS](#)
- Vissers, G. & Roupe van der Voort, L. 2012, ApJ, 750, 22 [ADS](#)
- Vissers, G. J. M., Roupe van der Voort, L. H. M., Rutten, R. J., Carlsson, M., & De Pontieu, B. 2015, ApJ, 812, 11 [ADS](#)
- Wilhelm, K., Curdt, W., Marsch, E., et al. 1995, SoPh, 162, 189 [ADS](#)
- Yurchyshyn, V., Abramenko, V., Kosovichev, A., & Goode, P. 2014, ApJ, 787, 58 [ADS](#)